iScience

Article

Boosting flexible laser-induced graphene supercapacitors performance through double pass laser processing

Graphical abstract

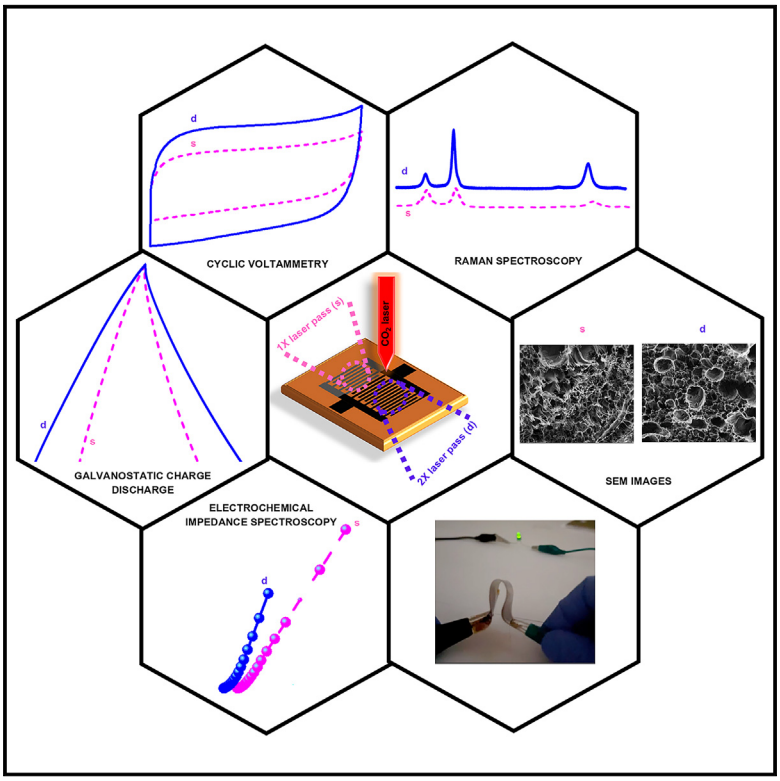

Highlights

- Double pass increased the pore size and the degree of graphitization of LIG
- Double pass enhanced the energy density from 0.77 to 2.20 μWh/cm^2 at 0.05 mA/cm^2
- The equivalent series resistance dropped from 197 to 78 Ω after a double pass
- Double pass supercapacitor showed 91% of capacitance retention after 10.000 cycles

Authors

Assia Hamada, Yu Kyoung Ryu, Andres Velasco, María Belén Gómez-Mancebo, Sergio Fernández Carretero, Fernando Calle, Javier Martinez

Correspondence

y.ryu@upm.es (Y.K.R.), javier.martinez@upm.es (J.M.)

In brief

Energy storage; Supercapacitors

Hamada et al., 2025, iScience *28*, 111696
January 17, 2025
https://doi.org/10.1016/j.isci.2024.111696

CellPress

iScience

CellPress
OPEN ACCESS

Article

Boosting flexible laser-induced graphene supercapacitors performance through double pass laser processing

Assia Hamada,[1] Yu Kyoung Ryu,[1,2,*] Andres Velasco,[1] María Belén Gómez-Mancebo,[3] Sergio Fernández Carretero,[4] Fernando Calle,[1,5] and Javier Martinez[1,6,7,*]

[1]Instituto de Sistemas Optoelectrónicos y Microtecnología, Universidad Politécnica de Madrid, Av. Complutense 30, 28040 Madrid, Spain
[2]Departamento de Física Aplicada e Ingeniería de Materiales, E.T.S.I Industriales, Universidad Politécnica de Madrid, C/José Gutiérrez Abascal 2, 28006 Madrid, Spain
[3]División de Química, Departamento de Tecnología, Centro de Investigaciones Energéticas, Medioambientales y Tecnológicas, Av. Complutense 40, 28040 Madrid, Spain
[4]Unidad de Residuos de Alta Actividad, Unidad de Fisión Nuclear, Centro de Investigaciones Energéticas, Medioambientales y Tecnológicas, Av. Complutense 40, 28040 Madrid, Spain
[5]Departamento de Ingeniería Electrónica, E.T.S.I Telecomunicación, Universidad Politécnica de Madrid, Av. Complutense 30, 28040 Madrid, Spain
[6]Departamento de Ciencia de Materiales-CIME, E.T.S.I Caminos, Canales y Puertos, Universidad Politécnica de Madrid, C/ Profesor Aranguren s/n, 28040 Madrid, Spain
[7]Lead contact
*Correspondence: y.ryu@upm.es (Y.K.R.), javier.martinez@upm.es (J.M.)
https://doi.org/10.1016/j.isci.2024.111696

SUMMARY

This study proposes a simple and cost-effective approach to enhance the performance of supercapacitors based on laser-induced graphene (LIG). The use of two consecutive laser passes using the same CO_2 engraver on polyimide film led to the expansion in the size of the pores, the increase in the graphitization degree, and the densification of the produced material. These changes in the morphology and chemical structure of the LIG impacted positively its electrochemical performance when it was used as an electrode for supercapacitors. The best achieved material displayed the following results: (a) an enhancement of the areal energy density from 0.77 to 2.20 $\mu Wh/cm^2$ at 0.05 mA/cm^2, (b) a reduction of 60% in the equivalent series resistance, (c) high cycling stability with a capacitance retention rate of 91% after 10.000 cycles, (d) high performance stability under mechanical tests at different angles, and (e) green LED illumination under configuration in series.

INTRODUCTION

During the last few years, the electronics sector has embarked on the production of a variety of intelligent and flexible devices—such as foldable smartphones, wearable health technology, microsensors, smart robots, Internet of Things (IoT), and self-charging devices.[1,2] This surge in electronic innovations has led to a huge demand for the next generation of flexible and miniaturized electrochemical energy storage (EES) devices.[3] Flexible microsupercapacitors are EES devices that meet lightweight and portable requirements. They offer many advantages, including exceptional mechanical flexibility, very high power, competitive energy density, rapid charging-discharging rates, a long cycle life, economic efficiency, and environmental friendliness.[3–5]

Since its development, laser-induced graphene produced by direct laser writing has become one of the most explored techniques for the fabrication of MSC electrodes.[6] It is low-cost and time effective since it enables the simultaneous synthesis of the material and patterning of the device geometry in a single step, clean room conditions are not required, and many inexpensive precursors are available.[4,7,8] Applying this technique, a three-dimensional porous network of graphene-like material is obtained, which presents high mechanical integrity, extensive porosity, large thermal stability, and efficient electric conductivity. The optimization of the fabrication process to obtain LIG with the highest quality is fundamental to maximizing the performance of the microsupercapacitors. The first step consists of the election of the precursor material: Kapton,[6] photoresist,[9] PEDOT,[10] lignin,[11] food components,[12,13] cork,[14] and plastic waste,[15] which are among the many organic materials that can be used to produce LIG electrodes. Given a precursor, different laser parameters can be adjusted to modulate the structure and properties of the generated electrode. The most frequently used parameters are the laser power, scan speed,[16–18] and focal distance.[19,20] Another explored parameter, and the focus of the present work, is the multiple laser passes. The increase in the number of passes increases the exposure time and the irradiated

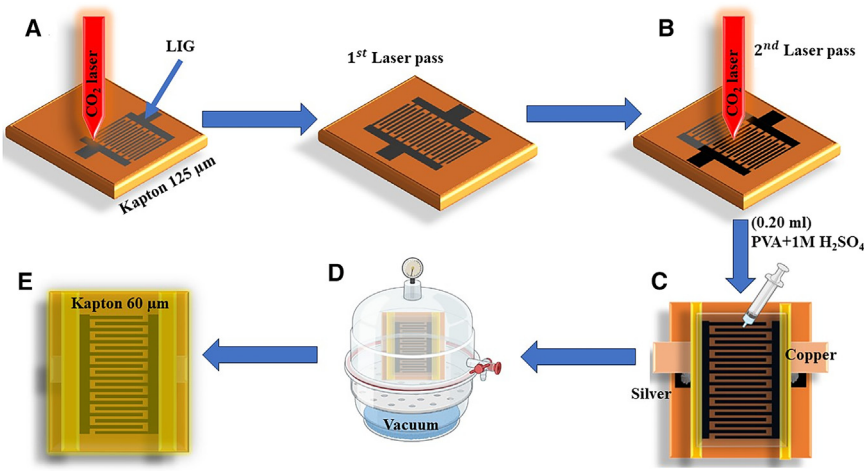

Figure 1. Scheme with the fabrication steps of an in-plane flexible LIG MSC

(A) The simultaneous patterning of the electrodes and transformation of Kapton into LIG was performed by laser writing (1st laser pass).

(B) The double pass samples underwent a second laser writing step, overlapping the first patterned electrodes (2nd laser pass).

(C) Assembly of the metallic current collectors with silver paint and copper, protection of the current collectors by adhesive Kapton, and subsequent application of the PVA:H_2SO_4 electrolyte on the active area of the electrodes.

(D) 1 h of active vacuum to remove the air inside the electrode pores and improve the electrolyte filling.

(E) Encapsulation with adhesive Kapton.

area, contributing to a more extensive carbonization process and the densification of LIG. This strategy has been utilized in prior studies to improve the LIG surface and its electrochemical properties by incorporating additional dopants or precursors between the pyrolysis steps[21–23] or by applying a defocusing technique to increase the laser spot size, achieving multiple irradiation times through overlapping.[12] In contrast, our target in this work was to demonstrate that the repetition of the irradiation step on a 125 μm thick Kapton film enabled the fabrication of pristine LIG-based supercapacitors with high-performance using the same CO_2 laser and the same fabrication parameters of power, scan rate and focal distance, without adding other materials. The generated materials were evaluated by different characterization methods, including scanning electron microscopy and X-ray diffraction analyses, Raman spectroscopy, and wettability tests. Once the conditions to produce the best double pass LIG electrode were determined, which corresponded to 2.4 W and 80 mm/s, in-plane flexible MSCs based on this LIG were fabricated. These devices exhibited a remarkable decrease of 60% in the equivalent series resistance and showcased notable improvements in the areal capacitance, from 3 to 8.12 mF/cm^2, and the energy density, from 0.77 to 2.20 μWh/cm^2, both measured at 0.05 mA/cm^2. They demonstrated excellent cycling stability, retaining 91% of its performance after 10.000 cycles at 0.5 mA/cm^2. Under mechanical deformation at different bending angles, their high flexibility and working robustness were verified. Three of these devices were assembled in a series configuration to switch on a green LED. Through the provided results, we have proposed a cost-effective and straightforward method for producing high quality LIG-based flexible microsupercapacitors by applying a double laser pass technique using the same tool.

RESULTS AND DISCUSSION

Flexible laser-induced graphene MSC fabrication

Regarding the acid gel electrolyte, it was prepared by adding 1 g PVA to a 20 mL mixture of 1M H_2SO_4 and DI water. Then, the solution was stirred at room temperature at 650 rpm on a hot plate magnetic stirrer. After 30 min, the temperature was increased to 75°C, and the solution was kept under continuous stirring for another 150 min until it became transparent and homogeneous.

The 125 μm thick Kapton film surface underwent an initial cleaning step with ethanol and subsequent drying using N_2. It was then subjected to CO_2 laser irradiation under ambient conditions to transform the initial polyimide into interdigitated LIG electrodes through an X-Y computer control system. The distance between the laser and Kapton was maintained at the focal length of 8 mm and the focused beam diameter was measured to be 100 μm. The used scan speed corresponded to 80 mm/s. Three different laser powers were used, namely 2.0, 2.4, and 2.8 W. Throughout the text, the name of the fabricated samples has the following nomenclature: *xLIG-y*, where *x* corresponds to "s" or "d," referring to single and double laser pass, respectively; and *y* represents the laser power. Therefore, the samples fabricated after a single pass and different powers correspond to: sLIG-2.0, sLIG-2.4, and sLIG-2.8. In the same way, the samples produced after two passes and different powers are denominated as dLIG-2.0, dLIG-2.4, and dLIG-2.8. A summary of the six studied samples as a function of the writing parameters can be found in Table S1 (supplemental information).

In Figure 1, a scheme with the fabrication steps of the in-plane LIG MSC is depicted. The electrode pair consists in 20 interdigitated fingers, with the dimensions specified in Figure S1 (supplemental information). The design of these electrodes was crafted using an open source vector image editing software, Inkscape. Then, it was transmitted to the laser via a control software (K40 Whisperer) and engraved on the Kapton substrate by the laser's continuous movement along the x-direction, with a constant y-line spacing of 75 μm (Figure 1A). In the case of the double pass samples, the laser engraving process was repeated a second time, overlapping the writing on the first generated LIG pattern, as shown in Figure 1B. Once the LIG electrodes were produced, the assembly of the components was carried out to fabricate the final device. First, the copper tape was placed on the squared-shaped endpoints of the electrodes to define the current collectors, with a drop of silver paint between the copper tape and the LIG to enhance the electrical contact. Then, the

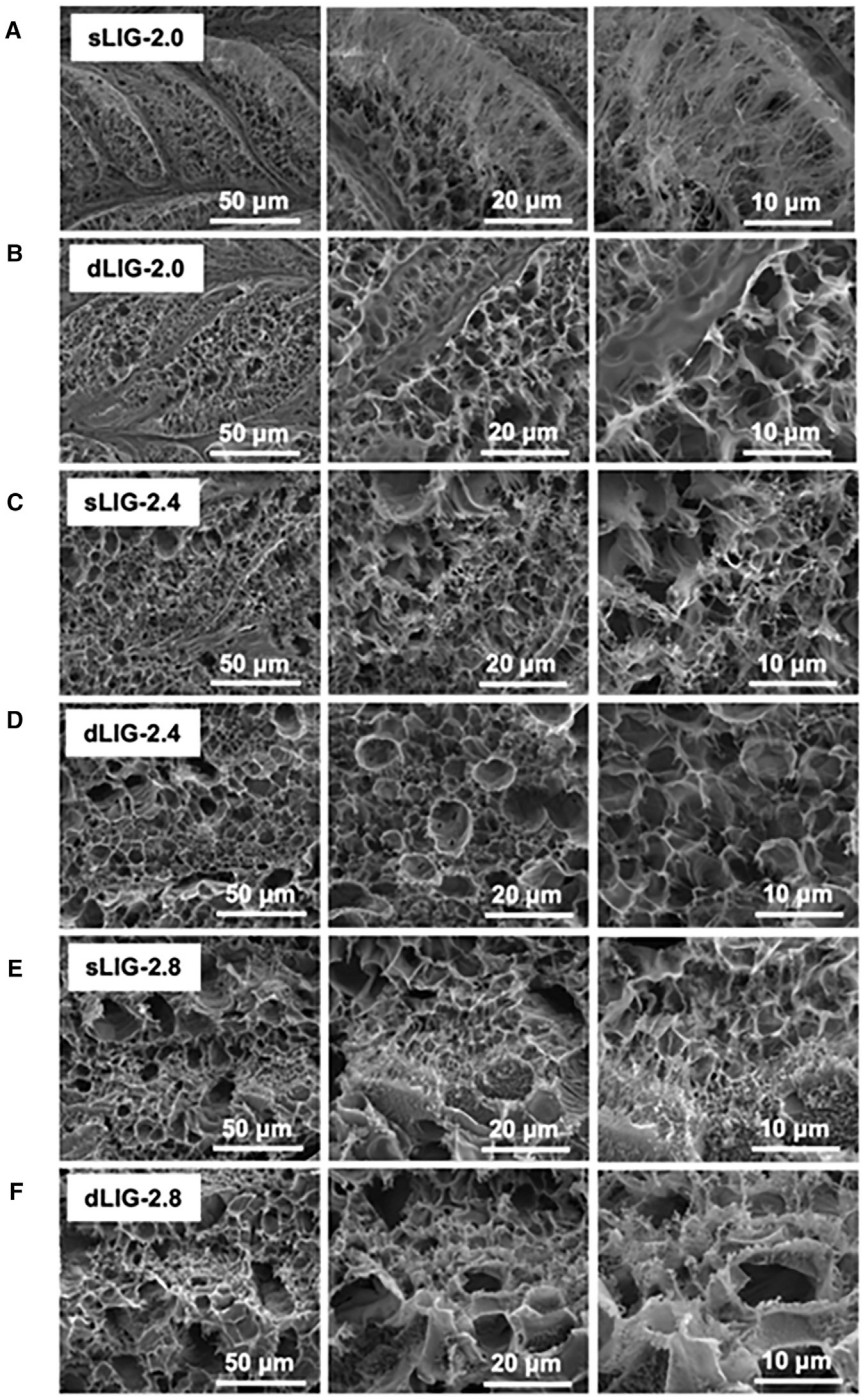

Figure 2. SEM images of single and double laser pass LIG materials

SEM images at three different scales and magnifications are presented: 50 μm, x2.000 (left column); 20 μm, x5.000 (center column); and 10 μm, x10.000 (right column).

(A) sLIG-2.0 (B) dLIG-2.0 (C) sLIG-2.4 (D) dLIG-2.4 (E) sLIG-2.8 (F) dLIG-2.8.

current collectors were covered by 60 μm thick adhesive Kapton stripes to isolate them and in this way, protect them from the acidic electrolyte. Finally, 0.20 mL of gel electrolyte was applied to the LIG active area (Figure 1C). After the assembly of the components, the device was placed under an active vacuum for 1 h to remove the air trapped inside the pores of the electrodes and therefore, to maximize their filling with the electrolyte (Figure 1D). Finally, the encapsulation step of the device by 60 μm thick adhesive Kapton film was performed, as represented in Figure 1E, obtaining the completed microsupercapacitor.

Laser-induced graphene electrodes characterization

The application of laser induces a localized temperature (>2500°C) that breaks the C – O, C = O, and N – C bonds of the Kapton film. The liberated atoms are released quickly as gases that create the pores and open sites on the LIG surface. Concurrently, the C atoms undergo a rearrangement to form graphitic structures.[6,18] The resulting morphology of the LIG varies as a function of the laser writing parameters. For instance, the increase in the laser power correlates with an augmentation in pore size, number, and density, as evidenced by numerous studies.[6,17,19,24] Figure 2 presents SEM images of LIG obtained with the three powers (2.0, 2.4, and 2.8 W) after single and double laser exposure. From the images corresponding to the lowest magnification (Figure 2, left column), it can be observed that the characteristic C or S shapes reflecting the scribing direction on the LIG surface fade progressively with the increase in power and number of passes due to the extension of the irradiated area. For the smallest laser power of 2.0 W and single pass, the LIG surface exhibits open sites rather than a network of pores and the predominant features consist of fibers (Figure 2A, center). By applying the second laser pass under the same power, the forest of fibers is replaced by a more porous structure as shown in Figure 2B, center. Figure 2C corresponds to a sample fabricated under a higher power of 2.4 W and single pass. It presents a more homogeneous structure with a higher average size of the pores (Figure 2C, center) and a smaller number of fibers. After two laser passes at 2.4 W, as presented in Figure 2D, center, the average size of the pores increased further, and a homogeneous LIG with a 3D foam structure was achieved. Figures 2E and 2F present the SEM images of the samples fabricated under the highest laser

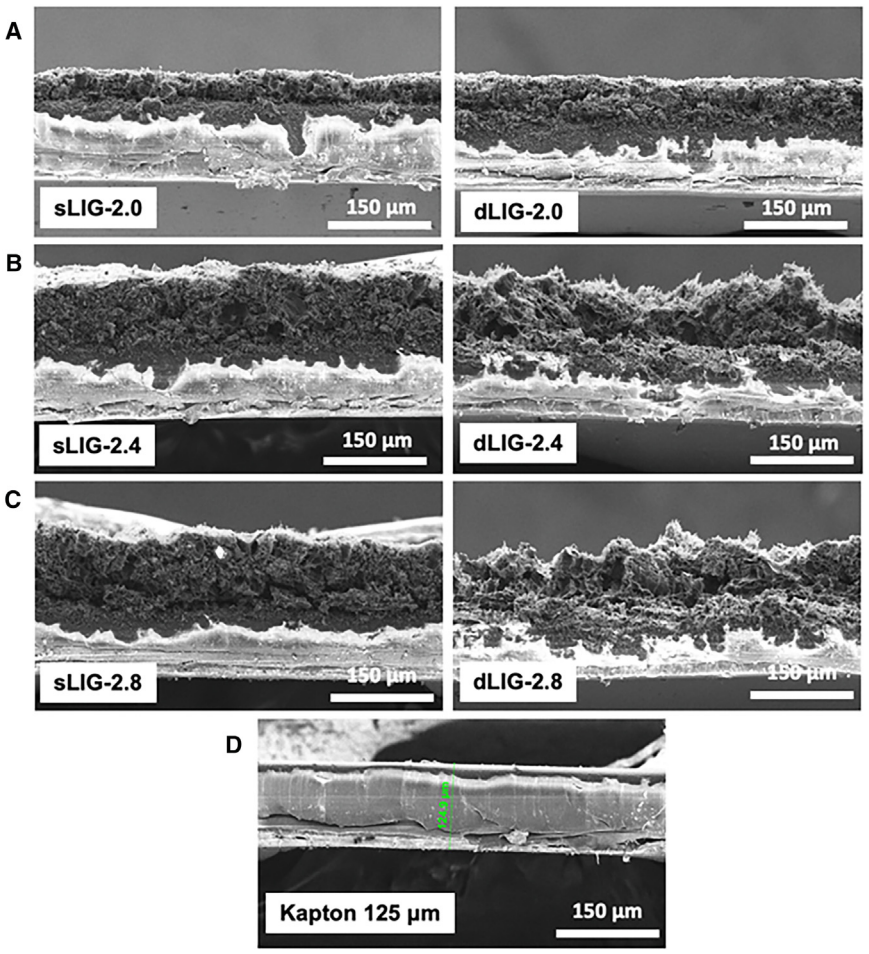

Figure 3. Cross-sectional SEM images of the produced LIG after different processing conditions

(A) Power: 2.0 W. Single pass (left) and double pass (right).

(B) Power: 2.4 W. Single pass (left) and double pass (right).

(C) Power: 2.8 W. Single pass (left) and double pass (right).

(D) Unprocessed 125 μm thick Kapton film. All the figures are at the same scale, with a value is 150 μm.

power of 2.8 W by single and double pass, respectively. Both samples present the biggest average size of the pores regarding the whole series. The effect of the double pass on the LIG structure can be clearly explained from the SEM images corresponding to the highest magnification (Figure 2, right column): the number of fibers decreases, replaced by thin flakes that form a dense network of big pores. To quantify the increase in the size of the pores, the distribution of pores sizes from the N_2 adsorption-desorption isotherms was evaluated by the Barrett-Joyner-Halenda method. The N_2 adsorption-desorption isotherms plots of all the samples are shown in Figure S2 and the results of the textural analysis are displayed in Table S2 (supplemental information). From Figure S2, it is highlighted that most of the nitrogen adsorption isotherms are type IV according to the IUPAC[25] and refer to mesoporous materials. The average pore widths presented in Table S2, which are inside the range of 3.58–4.50 nm, correspond in all cases to mesoporous materials according to IUPAC classification,[26] which states that mesoporous is between 2 and 50 nm. From Table S2, it can be observed that the adsorption average pore width, the adsorption average pore diameter, and the desorption average pore diameter values increased after the second pass for the three laser powers used in this work. Finally, the increase in the hydrophilicity of the samples with the increase in the size of the pores was confirmed after the performance of wettability tests, which results are shown in Figure S3 (supplemental information): For the three employed values of the laser power: 2.0, 2.4, and 2.8 W, the water contact angle with the surface decreases on the double pass LIG materials.[18,27] This result is beneficial for the use of LIG as microsupercapacitor electrodes since the increase in the size of the pores enhances the penetration and absorption of the electrolyte inside the active area of the electrode.

The effect of the double pass method on the thickness and the width of the produced LIG electrodes was also studied as displayed in Figures 3 and S4 (supplemental information), respectively. In Figure 3, SEM images with the cross-section of the fabricated LIG samples (Figures 3A–3C) and a piece of unmodified Kapton film (Figure 3D) are presented. In Figure 3D, the thickness of Kapton that was not irradiated by laser, corresponding to the initial 125 μm, was highlighted in green line in order to track with more clarity the changes in the material as a function of the number of laser passes. Focusing first on the applied power, the higher the value (from Figure 3A row to Figure 3C row), the laser penetration depth increases, represented as the growth in the thickness of the LIG surface and the reduction in the thickness of the initial Kapton film. The impact of a double pyrolysis step (Figures 3A–3C, right column) was an increase in the amount of transformed Kapton, represented as the increase in the LIG thickness of 36% for 2.0 W, of 18% for 2.4 W, and of 13% for 2.8 W, comparing with the corresponding samples fabricated using only one lasing step (Figures 3A–3C, left column). Due to the corrugated surface of the material, average thickness values from the cross-section images were taken for all the samples. In the case of the sample dLIG-2.8 (Figure 3C, right image), it is observed that the amount of material transformed from Kapton to LIG is very high, but the loss of LIG material is significant as well and the thickness of the left unmodified Kapton film is very small, which compromises the integrity and stability of the substrate on which the LIG electrode lies to use it as a functional

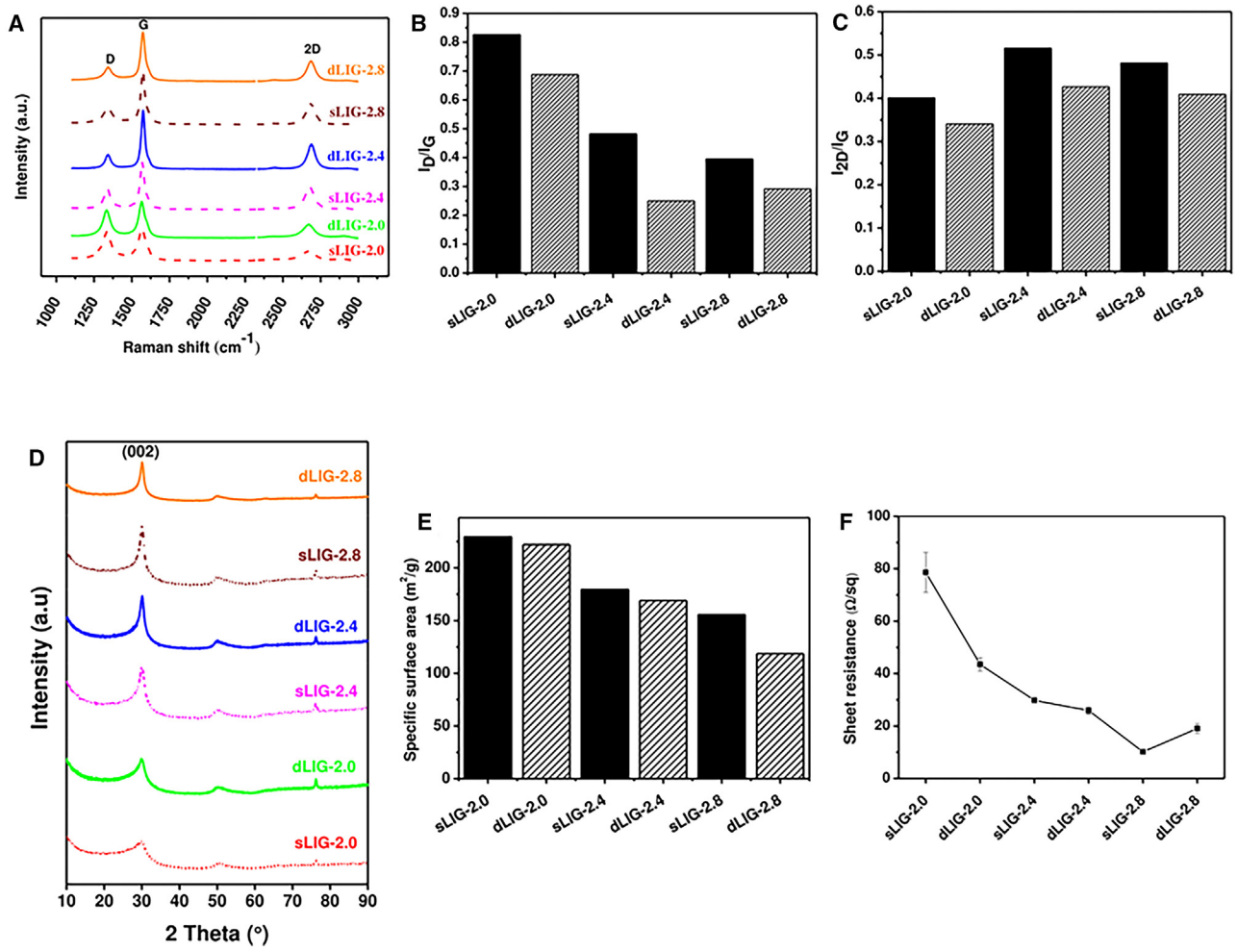

Figure 4. Structural, chemical, and electrical characterization of the studied LIG samples

(A) Raman spectra, where the 3 main graphene peaks: D, G, and 2D, can be observed.

(B) Graph where the I_D/I_G ratios are represented.

(C) Graph displaying the I_{2D}/I_G ratios.

(D) XRD analysis spectra.

(E) Specific surface area of the samples through BET analysis.

(F) Sheet resistance of the studied LIG samples. Each point corresponds to an average value of three samples, including their standard deviation represented as the vertical error bars. All the spectra in (A) and (D) are represented at the same scale, but they are just displaced along the vertical direction to facilitate their visualization and comparison.

device. The conclusion is that the power value of 2.8 W starts to be too high for applying a second laser pass. The results presented in Figure 3 prove that a double lasing process yields the densification of the LIG electrode. The increase in the lasing power and the number of passes also produces an increase in the width of the electrode fingers, as measured from the optical images displayed in Figure S4 (supplemental information). This means an increment in the active area and a decrease in the distance between the fingers, which facilitates faster ions movement and improves the capacitance of the electrical double-layer mechanism when the in-plane MSC is considered under the parallel-plate capacitor model.[28]

The chemical composition of the fabricated LIG materials was investigated using several spectroscopic techniques. The results are summarized in Figure 4. The Raman spectra of the six studied samples, shown in Figure 4A, exhibit the three main Raman peaks corresponding to graphene-based materials: D, G, and 2D peaks, centered around 1333 cm^{-1}, 1570 cm^{-1} and 2670 cm^{-1}, respectively.[29,30] A gradual decrease in the intensity of the D peak and an increase in the intensity of the G and 2D peaks as a function of the power and number of passes can be observed. Figure 4B presents the I_D/I_G ratio between D and G peak intensities for each sample. The three samples that underwent a second laser pass present a lower I_D/I_G ratio compared to their single laser pass counterparts, which is associated with a lower defect density and a higher degree of graphitization.[12,24] Specifically, dLIG-2.4 displays the lowest I_D/I_G ratio, indicating the highest quality LIG material. The I_D/I_G ratios

corresponding to sLIG-2.8 and dLIG-2.8 are inside the range of values between the ones from sLIG-2.4 and dLIG-2.4. This indicates that for the used scan speed of 80 mm/s, 2.8 W of power starts to affect the integrity of the LIG microstructure.[17] The graph from Figure 4C displays the I_{2D}/I_G ratio for each sample, related to the number of graphene layers formed in the LIG material. This ratio falls within the narrow range of 0.3–0.5, indicating that all the produced materials consist of a porous network of multilayer graphene films with few layers, approximately 4–5.[31]

Figure 4D shows the spectra obtained from the XRD analysis using Co Kα radiation (λ = 1.789 Å). As a result, the (002) diffraction peak center appeared in the range of 28°-29°, instead of between 25° and 26°, which is observed when Cu Kα radiation (λ = 1.54 Å) is employed.[6] The increase in the lasing power and the number of laser passes led to the gradual increase of the (002) diffraction peak intensity and also to the gradual shift of the (002) diffraction peak center from 28.20° to 29.85°, which translates into the shift of the interlayer distance from 3.67 to 3.47 Å, calculated using Bragg's formula.[32] The specific values of the (002) diffraction peak center and the corresponding interlayer distance for each type of sample can be found in Table S3 (supplemental information). The interlayer spacing of graphite corresponds to 3.36 Å.[33] Therefore, the result from the XRD analysis demonstrated an increase in the level of graphitization starting from sLIG-2.0 to dLIG-2.8.

The specific surface area (SSA) of the six samples studied was estimated via the Brunauer-Emmett-Teller method, whose values are illustrated in Figure 4E. The SSA decreases with the increase of the laser power since the rise of this parameter leads to a higher degree of graphitization, but also, a higher material loss.[17,24] Regarding the influence of multiple passing on the produced LIG, it can be observed from the textural analysis displayed in Table S2 (supplemental information) that the SSA decreases and the BJH adsorption and desorption average pore diameters increase when a second laser pass is applied. These results underline a complex balance: a double pass increases the degree of graphitization and the pore size, which are positive outcomes, but at the expense of reducing the SSA, which is a negative outcome. However, despite the drop in the SSA, the second pass step improved significatively the performance of the MSCs, as demonstrated later in the electrochemical characterization section, due to all the other achieved positive effects: (a) the densification of the electrodes, which leads to the gain of material per unit volume,[21,34] (b) the increase in the pore size, which leads to the increase in the hydrophilicity and (c) the increase in the degree of graphitization, which leads to the increase in the material quality. Therefore, the potential use of the double pass technique to optimize the LIG-based electrodes is reaffirmed. Finally, for the samples fabricated under 2.8 W, the excessive loss of SSA after the second pass indicates again that the power value is too high, as it was deduced from the SEM cross sectional images (Figure 3) and the Raman analysis results (Figures 4A–4C).

To characterize the electrical properties of the studied samples, the value of their sheet resistance was determined by the four-point probe technique, represented in Figure 4F. In the case of the samples fabricated under 2.0 and 2.4 W, the sheet resistance decreased after the second pass, from 78.6 to 43.5 Ω/sq and 29.8 to 25.9 Ω/sq, respectively. This improvement in the electrical conductivity of the samples indicates the production of LIG with better quality after the second pass. However, for the samples fabricated under 2.8 W, the sheet resistance worsened from 10.2 (single pass) to 19.0 (double pass) Ω/sq. This result confirms once more that 2.8 W of power is too high and damages the integrity of the LIG microstructure,[17] which is reflected in the increase of the sheet resistance value. Regarding the sheet resistance values of all the studied samples, they are inside the range of the measured values from LIG fabricated using a CO_2 laser and polyimide as a precursor in previous works.[35–37]

Double pass laser-induced graphene MSCs electrochemical performance

Flexible LIG microsupercapacitors based on the six conditions considered in the present work were fabricated, using 1M H_2SO_4:PVA gel electrolyte, to investigate the impact of the double pass technique on the performance of the device. For the electrochemical characterization, cyclic voltammetry, charge-discharge, and electrochemical impedance spectroscopy curves were measured, as shown in Figure 5. To enable the comparison, all the graphs were represented under the same X and Y scales. The CV curves depicted in Figure 5A were measured under a scan rate of 0.02 V/s. The rest of the profiles at different scan rates are shown in Figure S5 (supplemental information). All of them exhibit symmetric quasi-rectangular shapes across all the devices, a characteristic feature of electric double-layer capacitors (EDLCs), which indicates a good electrochemical stability within the range of the used lasing conditions. For the three power values of 2.0, 2.4, and 2.8 W, a second laser pass improves the performance of the supercapacitors: the current density increases, and consequently, the area enclosed under the CV curve, which represents the total amount of stored charge. This result confirms the beneficial role of the multiple lasing to obtain a better LIG material.

A parallel observation can be drawn from the GCD curves measured under a current density of 0.05 mA/cm^2, shown in Figure 5B, where the samples that underwent a second pass step present more symmetric triangular shapes and longer charge and discharge times, indicating an improvement in the capacitive behavior. The rest of the curves at different current densities are depicted in Figure S6 (supplemental information). Among all the studied samples, dLIG-2.4 achieves the largest CV curve area (Figure 5A, center) and the best GCD curve (Figure 5B, center), indicative of the highest capacitance.

EIS analysis was performed on the devices, and the high frequency region of the Nyquist plots is represented in Figure 5C to show more clearly the intercept of the curve in the axis of the real component Z′ of the impedance, which corresponds to the electrode resistance value. From Figure 5C, it can be observed that the two laser pass samples present smaller electrode resistances compared to the single pass ones for all the used powers. The EIS curves with the full range of measured frequencies are represented in Figure S7 (supplemental information). Finally, the equivalent series resistance (ESR) of the electrolyte-electrode system for all the samples was calculated

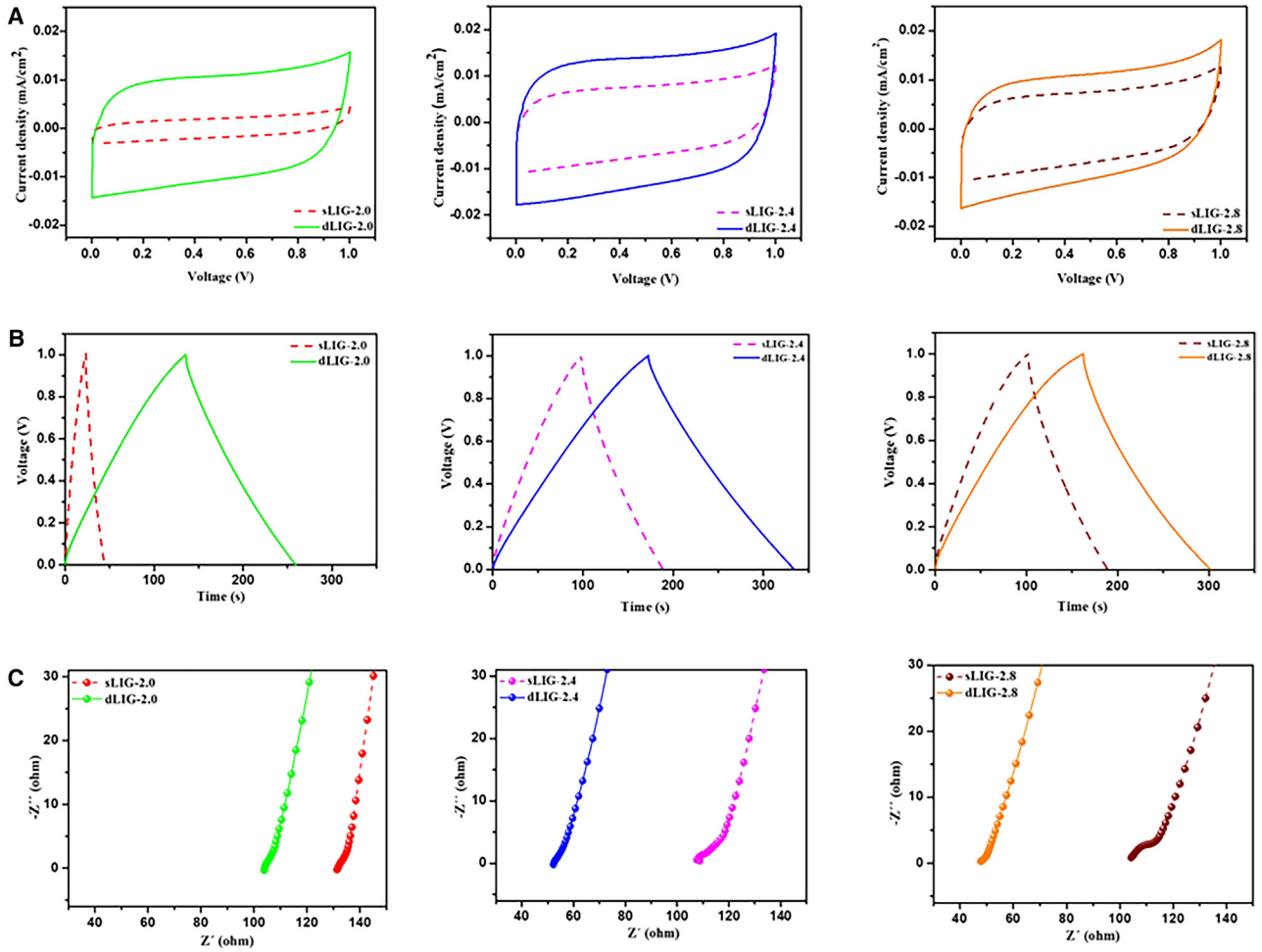

Figure 5. Comparative electrochemical performance analysis of single and double laser pass devices

(A) CV at 0.02 V/s.

(B) GCD at 0.05 mA/cm^2.

(C) Electrochemical impedance spectroscopy measurements. Black curves represent single-pass samples, while blue curves depict double-pass samples. The samples, corresponding to 2.0 W, 2.4 W, and 2.8 W, are presented from left to right for each case.

using the Equation 4, described in the method details. The ESR drops from 217 (sLIG-2.0) to 96 (dLIG-2.0) ohms; from 197 (sLIG-2.4) to 78 (dLIG-2.4) ohms, and from 160 (sLIG-2.8) to 84 (dLIG-2.8) ohms, when a double pass is applied. The second pass, as described above, widens the fingers of the in-plane MSC electrodes, reducing the gap between them, and producing a densification of the LIG structure. These outcomes contribute to the reduction of the device resistance.

To provide the comparative assessment of the fabricated MSCs, the areal capacitance versus current density and the Ragone plots (energy density versus power density graphs) are presented in Figures 6A and 6B, respectively. The values were calculated using the Equations 1, 2, and 3, presented in method details. The dashed line curves refer to single laser pass samples and the continuous line curves, to second pass ones. The values of capacitance, energy, and power given in the following discussion correspond to a current density of 0.05 mA/cm^2. The dLIG-2.4 sample stands out with the highest areal capacitance, exhibiting an increase from 3 to 8.12 mF/cm^2 when compared with sLIG-2.4 (pink versus blue curves in Figure 6A). Correspondingly, the energy density experiences a substantial boost from 0.77 to 2.20 μWh/cm^2 (pink versus blue curves in Figure 6B). For the sLIG-2.8 and dLIG-2.8 pair of samples, there is also a marked improvement when a second pass is applied, demonstrating an increase in the areal capacitance from 2.55 to 7.56 mF/cm^2 (brown versus orange curves in Figure 6A). Simultaneously, the energy density rises from 0.67 to 2.03 μWh/cm^2 (brown versus orange curves in Figure 6B). Comparing the sLIG-2.0 and dLIG-2.0 samples, the second one exhibits an enhancement in the areal capacitance, from 2.25 to 6.68 mF/cm^2 (red versus green curves in Figure 6A), accompanied by an increment in the energy density from 0.58 to 1.79 μWh/cm^2 (red versus green curves in Figure 6B). The fundamental conclusion of these results is the appreciable increase in the energy density of the devices when two lasing steps are performed. This emphasizes the substantial impact of improving the LIG quality on enhancing the performance of the

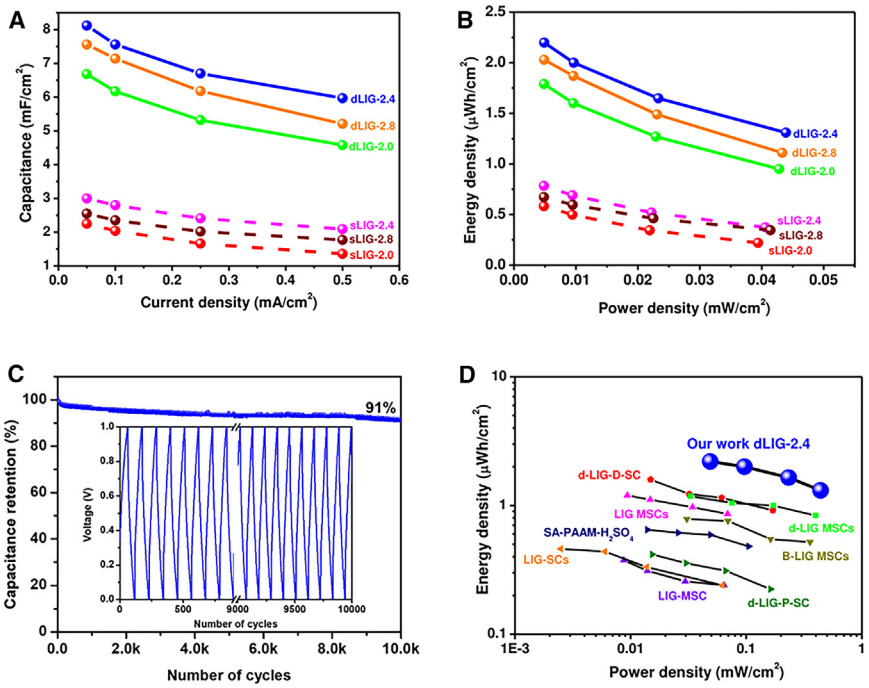

Figure 6. Performance analysis of single and double laser pass devices

(A) Comparison of the areal capacitance versus scan rates.

(B) Ragone Plot.

(C) Cycling test of dLIG-2.4 at 0.5 mA/cm^2 under 10.000 cycles. Capacitance was calculated from the GCD curves. The inset graph displays a few of the GCD cycles to illustrate the excellent stability of the measurements.

(D) Ragone plot where the best obtained MSC from our work, dLIG-2.4, is compared with similar devices obtained from other works in the field: B-LIG-MSCs,[38] d-LIG-MSCs,[22] SA-PAAM-H_2SO_4,[39] LIG-MSCs,[6] LIG-MSCs and LIG-SCs,[40] d-LIG-P-SC and d-LIG-D-SC.[21]

MSCs. The second pass treatment, as it was revealed by SEM, Raman, and XRD analyses, alters significantly the LIG morphology: it produces a structure densification, reduces defects, heightens the degree of graphitization, and facilitates the penetration of the electrolyte ions by pores opening. All these effects are translated into energy storage devices with better working characteristics. The cycling stability was tested using an MSC fabricated under the best parameters, corresponding to dLIG-2.4. The measurement presented in Figure 6C involved the continuous operation of the GCD process over 10.000 cycles at a current density of 0.5 mA/cm^2. The observed retention in the areal capacitance after the end of the process was approximately of 91%, showcasing a remarkable and enduring cycling stability over the extended period. The inset of Figure 6C displays a few of the first and last cycles of the cycling test to illustrate the reproducibility of the values during the test.

Figure 6D shows a Ragone plot comparing the best-achieved LIG-MSC in this work, dLIG-2.4, to a number of similar devices found in the literature using different processing: B-LIG MSCs boron-doped LIG flexible MSCs,[38] PAA coated d-LIG-MSCs,[22] sodium alginate/polyacrylamide LIG-MSCs,[39] pristine LIG-MSCs,[6] stackable LIG-MSCs,[40] and densified pristine and doped PAA-LIG-MSCs.[21] Among these microsupercapacitors, some of them are based only on bare LIG and others are based on LIG doped with pseudocapacitive materials. Our device, falling inside the first category, presents a higher energy density and higher or comparable power density values, which confirms the production of high-performance devices through the application of the double pass strategy.

Double pass laser-induced graphene based applications

In order to demonstrate the use of double pass LIG in potential applications, we checked first the transferability of the material to alternative substrates. In fields such as wearable electronics, where mechanical robustness, flexibility, and stretchability are crucial, transparent, and elastomeric materials serve as ideal substrates for device fabrication. An extended example is the creation of stretchable LIG-based strain sensors on a polydimethylsiloxane (PDMS) substrate.[11,41,42] Samples fabricated using the best conditions in the present work, dLIG-2.4, were successfully transferred onto PDMS as presented in Figure 7A, with the shape of the logo of our research institute, ISOM, which stands for Instituto de Sistemas Optoelectrónicos y Microtecnología (top panel); the in-plane electrodes design we used for our MSCs (bottom, left panel) and the logo of our university, Universidad Politécnica de Madrid (bottom, right panel). A transfer with high uniformity and sharply defined features was achieved. The Kapton films that contained the initial LIG, left after the transfer, are shown in Figure S8 (supplemental information). Furthermore, dLIG-2.4 MSCs exhibit a robust mechanical performance without notable compromise to their electrochemical storage properties. Throughout the bending process at various angles, shown in Figure 7B, the cyclic voltammetry curves of the device maintain overlapped, quasi-rectangular shapes, proving both high flexibility and remarkable stability under deformation. This result suggests that the device retains its structural and electrochemical integrity even when subjected to mechanical stress, reinforcing its suitability for flexible applications without significant degradation in performance.

Moreover, three dLIG-2.4 devices were placed in series and in parallel to record the increase of the potential window and the capacitance, respectively, as shown in Figures 7C and 7D. Compared to a single device (blue curves), the series system shows a larger potential difference (red curves), while the parallel connection results in an increase in the current (black curves). To delve deeper into the capabilities of double pass LIG MSCs for flexible applications, a device consisting of three dLIG-2.4 MSCs in series was employed to expand the voltage window up to 3 V, aligning with the specifications of a green LED. The power unit derived from the dLIG-2.4 in series configuration proved readily available to sustain LED illumination for approximately 47 s, even when subjected to multiple manual

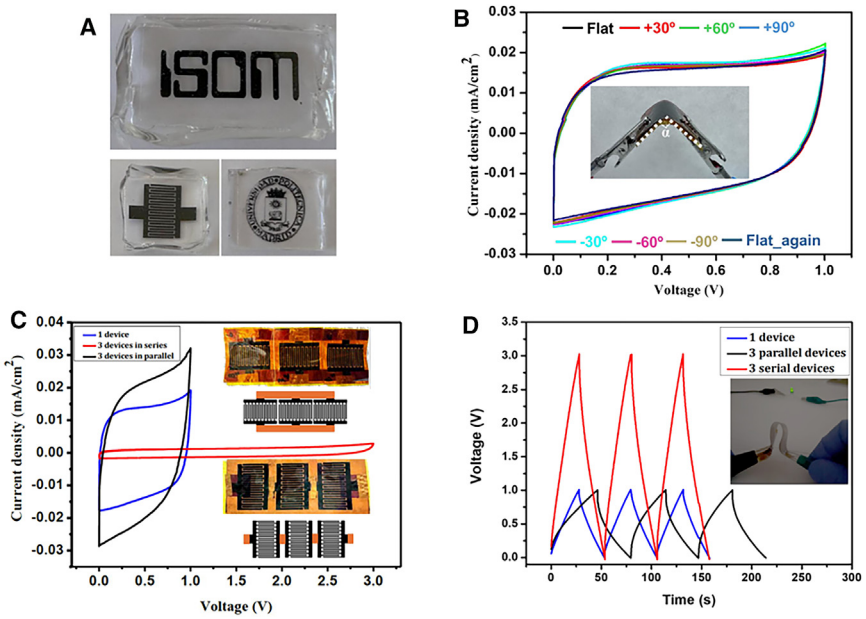

Figure 7. Proof-of-concept tests using dLIG-2.4

(A) Examples of dLIG-2.4 after transfer to PDMS. ISOM logo (top), in-plane MSC Design used in this work (bottom left), and UPM logo (bottom right).

(B) CV tests performed using a dLIG-2.4 MSC at 0.02 V/s under different bending angles.

(C) CV and (D) GCD analysis of different dLIG-2.4 MSCs: single device (blue line), series connection of three devices (red line), and parallel arrangement of three devices (black line). Inside the graph shown in (C), pictures of the parallel device (top) and the in series device (bottom), with their respective circuit schemes later in discussion, are presented.

bending actions. The corresponding movie illustrating these results is provided as Video S1 (supplemental information). These findings underscore the suitability of these flexible LIG-MSCs for powering flexible and portable electronics as portable energy sources.

Conclusion

In summary, this study introduces a fast and cost-effective approach to fabricating in-plane, flexible MSCs through a direct laser writing process on a 125 μm thick Kapton film by employing a double laser pass technique using the same tool. Thanks to the multiple lasing approach, the outcoming LIG electrode material exhibits an enhanced quality through (a) a high graphitization degree, (b) the structure densification, (c) the augmentation of the pore size, which eases the infiltration of the electrolyte inside the electrodes, and (d) the widening of the fingers and subsequent reduction of the gap between them, which translates into an increase in the active area and electrical conductivity, respectively. The best LIG material was obtained under the following laser conditions: 2.4 W, 80 mm/s, and double pass. The devices fabricated using this LIG, dLIG-2.4, showcase an enhancement in their electrochemical performance with respect to their single pass counterparts: an improvement of the areal capacitance from 3 to 8.12 mF/cm^2, and an energy density boost from 0.77 to 2.20 μWh/cm^2, both referred to a current density value of 0.05 mA/cm^2 and a decrease of 60% in the equivalent series resistance. Moreover, the dLIG-2.4 based MSCs exhibited exceptional results: (a) An excellent cycling stability, maintaining 91% of their performance even after 10.000 cycles at 0.5 mA/cm^2; (b) high stability and mechanical flexibility under different bending angles; (c) successful transferability to PDMS substrate; (d) and successful energy supply to switch on a green LED under in series configuration. These outcomes prove the potential of this LIG fabrication strategy for versatile and resilient energy storage applications, addressing the demands of modern, flexible electronics.

Limitations of the study

The implementation of two laser passes on a 125 μm thick polyimide film using the same CO_2 laser and the same writing parameters of power, scan rate and focal distance has a significant influence on the final morphology and electrochemical performance of the produced laser-induced graphene. In the present work, the main limitation was posed by the given thickness of the commercial film, which restricted the number of applicable laser passes, hindering the further material engineering. However, this study has opened the potential to explore the optimal number of laser irradiation reiterations in other precursors with different thicknesses to obtain the laser-induced graphene with the best properties.

RESOURCE AVAILABILITY

Lead contact

Requests for further information and resources should be directed to and will be fulfilled by the lead contact, Javier Martínez Rodrigo (javier.martinez@upm.es).

Materials availability

This study did not generate new unique reagents.

Data and code availability

- All data generated and/or analyzed during this study are included in the article and supplementary figures and tables.
- This article does not report original code.
- Any additional information required to reanalyze the data reported in this article is available from the lead contact upon request.

ACKNOWLEDGMENTS

This work has received funding from the Spanish Ministry of Science and Innovation (MICINN) through projects grants PID2020-114234RB-C21 and -C22

funded by MCIN/AEI/10.13039/501100011033; from the Comunidad de Madrid, the Recovery, Transformation and Resilience Plan of the Spanish Government and the European Union - NextGenerationEU (PRTR-C17.I1) project MAD2D-CM-UPM1 (Complementary Plan for Advanced Materials); and from the MIT-Spain Inditex Circularity Seed Fund.

ERDF is also gratefully acknowledged for the partial funding of the XRD equipment employed for this study (Project FEDER 2004 CIEM05-34-031).

AUTHOR CONTRIBUTIONS

A. H.: Conceptualization, data curation, formal analysis, investigation, methodology, writing-original draft, and writing-review and editing. Y. K. R.: Data curation, formal analysis, investigation, methodology, supervision, writing-original draft, and writing-review and editing. A. V.: Data curation, investigation, methodology, and writing-review and editing. M. B. G.-M.: Investigation, data curation, and writing-review and editing. S. F. C.: Investigation, data curation, and writing-review and editing. F. C.: Writing-review and editing. J. M.: Investigation, supervision, validation, writing-review and editing, and funding acquisition.

DECLARATION OF INTERESTS

The authors declare no competing interests.

STAR★METHODS

Detailed methods are provided in the online version of this paper and include the following:

- KEY RESOURCES TABLE
- METHOD DETAILS
  - Materials
  - LIG electrodes characterization methods
  - Supercapacitors electrochemical characterization
  - Process of LIG transfer to PDMS substrate
- QUANTIFICATION AND STATISTICAL ANALYSIS

SUPPLEMENTAL INFORMATION

Supplemental information can be found online at https://doi.org/10.1016/j.isci.2024.111696.

Received: July 31, 2024
Revised: December 3, 2024
Accepted: December 23, 2024
Published: December 26, 2024

REFERENCES

1. Shi, Q., Dong, B., He, T., Sun, Z., Zhu, J., Zhang, Z., and Lee, C. (2020). Progress in wearable electronics/photonics—Moving toward the era of artificial intelligence and internet of things. Inf. Manage. *2*, 1131–1162. https://doi.org/10.1002/inf2.12122.
2. Liu, R., Wang, Z.L., Fukuda, K., and Someya, T. (2022). Flexible self-charging power sources. Nat. Rev. Mater. *7*, 870–886. https://doi.org/10.1038/s41578-022-00441-0.
3. Lee, J.-H., Yang, G., Kim, C.-H., Mahajan, R.L., Lee, S.-Y., and Park, S.-J. (2022). Flexible solid-state hybrid supercapacitors for the internet of everything (IoE). Energy Environ. Sci. *15*, 2233–2258. https://doi.org/10.1039/D1EE03567C.
4. Wan, Z., Chen, X., and Gu, M. (2021). Laser scribed graphene for supercapacitors. Opto-Electron. Adv. *4*, 200079. https://doi.org/10.29026/oea.2021.200079.
5. Bu, F., Zhou, W., Xu, Y., Du, Y., Guan, C., and Huang, W. (2020). Recent developments of advanced micro-supercapacitors: design, fabrication and applications. Npj Flex. Electron. *4*, 31. https://doi.org/10.1038/s41528-020-00093-6.
6. Lin, J., Peng, Z., Liu, Y., Ruiz-Zepeda, F., Ye, R., Samuel, E.L.G., Yacaman, M.J., Yakobson, B.I., and Tour, J.M. (2014). Laser-induced porous graphene films from commercial polymers. Nat. Commun. *5*, 5714. https://doi.org/10.1038/ncomms6714.
7. Ma, W., Zhu, J., Wang, Z., Song, W., and Cao, G. (2020). Recent advances in preparation and application of laser-induced graphene in energy storage devices. Mater. Today Energy *18*, 100569. https://doi.org/10.1016/j.mtener.2020.100569.
8. Ye, R., James, D.K., and Tour, J.M. (2019). Laser-Induced Graphene: From Discovery to Translation. Adv. Mater. *31*, 1803621. https://doi.org/10.1002/adma.201803621.
9. Beckham, J.L., Li, J.T., Stanford, M.G., Chen, W., McHugh, E.A., Advincula, P.A., Wyss, K.M., Chyan, Y., Boldman, W.L., Rack, P.D., and Tour, J.M. (2021). High-Resolution Laser-Induced Graphene from Photoresist. ACS Nano *15*, 8976–8983. https://doi.org/10.1021/acsnano.1c01843.
10. Cho, E.-C., Chang-Jian, C.-W., Syu, W.-L., Tseng, H.-S., Lee, K.-C., Huang, J.-H., and Hsiao, Y.-S. (2020). PEDOT-modified laser-scribed graphene films as bginder– and metallic current collector–free electrodes for large-sized supercapacitors. Appl. Surf. Sci. *518*, 146193. https://doi.org/10.1016/j.apsusc.2020.146193.
11. Mahmood, F., Zhang, H., Lin, J., Wan, C., and Wan, C. (2020). Laser-Induced Graphene Derived from Kraft Lignin for Flexible Supercapacitors. ACS Omega *5*, 14611–14618. https://doi.org/10.1021/acsomega.0c01293.
12. Chyan, Y., Ye, R., Li, Y., Singh, S.P., Arnusch, C.J., and Tour, J.M. (2018). Laser-Induced Graphene by Multiple Lasing: Toward Electronics on Cloth, Paper, and Food. ACS Nano *12*, 2176–2183. https://doi.org/10.1021/acsnano.7b08539.
13. Larrigy, C., Burke, M., Imbrogno, A., Vaughan, E., Santillo, C., Lavorgna, M., Sygellou, L., Paterakis, G., Galiotis, C., Iacopino, D., and Quinn, A.J. (2023). Porous 3D Graphene from Sustainable Materials: Laser Graphitization of Chitosan. Adv. Mater. Technol. *8*, 2201228. https://doi.org/10.1002/admt.202201228.
14. Silvestre, S.L., Pinheiro, T., Marques, A.C., Deuermeier, J., Coelho, J., Martins, R., Pereira, L., and Fortunato, E. (2022). Cork derived laser-induced graphene for sustainable green electronics. Flex. Print. Electron. *7*, 035021. https://doi.org/10.1088/2058-8585/ac8e7b.
15. Wyss, K.M., Beckham, J.L., Chen, W., Luong, D.X., Hundi, P., Raghuraman, S., Shahsavari, R., and Tour, J.M. (2021). Converting plastic waste pyrolysis ash into flash graphene. Carbon *174*, 430–438. https://doi.org/10.1016/j.carbon.2020.12.063.
16. Lamberti, A., Perrucci, F., Caprioli, M., Serrapede, M., Fontana, M., Bianco, S., Ferrero, S., and Tresso, E. (2017). New insights on laser-induced graphene electrodes for flexible supercapacitors: Tunable morphology and physical properties. Nanotechnology *28*, 174002. https://doi.org/10.1088/1361-6528/aa6615.
17. Velasco, A., Ryu, Y.K., Hamada, A., De Andrés, A., Calle, F., and Martinez, J. (2023). Laser-Induced Graphene Microsupercapacitors: Structure, Quality, and Performance. Nanomaterials *13*, 788. https://doi.org/10.3390/nano13050788.
18. Tiliakos, A., Ceaus, C., Iordache, S.M., Vasile, E., and Stamatin, I. (2016). Morphic transitions of nanocarbons via laser pyrolysis of polyimide films. J. Anal. Appl. Pyrolysis *121*, 275–286. https://doi.org/10.1016/j.jaap.2016.08.007.
19. Ruan, X., Wang, R., Luo, J., Yao, Y., and Liu, T. (2018). Experimental and modeling study of CO2 laser writing induced polyimide carbonization process. Mater. Des. *160*, 1168–1177. https://doi.org/10.1016/j.matdes.2018.10.050.
20. Abdulhafez, M., Tomaraei, G.N., and Bedewy, M. (2021). Fluence-Dependent Morphological Transitions in Laser-Induced Graphene Electrodes on

Polyimide Substrates for Flexible Devices. ACS Appl. Nano Mater. *4*, 2973–2986. https://doi.org/10.1021/acsanm.1c00101.

21. Ryu, C., Do, H.M., and In, J.B. (2024). Enhanced performance of densified laser-induced graphene supercapacitor electrodes in dimpled polyimide. Appl. Surf. Sci. *643*, 158696. https://doi.org/10.1016/j.apsusc.2023.158696.
22. Lee, J., Jang, J., Zhou, H., Lee, Y., and In, J. (2020). Densified laser-induced graphene for flexible microsupercapacitors. Energies *13*, 6567. https://doi.org/10.3390/en13246567.
23. Zhang, Q., Zhang, F., Liu, X., Yue, Z., Chen, X., and Wan, Z. (2023). Doping of laser-induced graphene and its applications. Adv. Mater. Technol. *8*, 2300244. https://doi.org/10.1002/admt.202300244.
24. Liu, M., Wu, J., and Cheng, H. (2022). Effects of laser processing parameters on properties of laser-induced graphene by irradiating CO2 laser on polyimide. Sci. China Technol. Sci. *65*, 41–52. https://doi.org/10.1007/s11431-021-1918-8.
25. Rahman, M.M., Muttakin, M., Pal, A., Shafiullah, A.Z., and Saha, B.B. (2019). A statistical approach to determine optimal models for IUPAC-classified adsorption isotherms. Energies *12*, 4565. https://doi.org/10.3390/en12234565.
26. White, R.J., Budarin, V., Luque, R., Clark, J.H., and Macquarrie, D.J. (2009). Tuneable porous carbonaceous materials from renewable resources. Chem. Soc. Rev. *38*, 3401–3418. https://doi.org/10.1039/B822668G.
27. Nasser, J., Lin, J., Zhang, L., and Sodano, H.A. (2020). Laser induced graphene printing of spatially controlled super-hydrophobic/hydrophilic surfaces. Carbon *162*, 570–578. https://doi.org/10.1016/j.carbon.2020.03.002.
28. Yan, J., Wang, Q., Wei, T., and Fan, Z. (2014). Recent Advances in Design and Fabrication of Electrochemical Supercapacitors with High Energy Densities. Adv. Energy Mater. *4*, 1300816. https://doi.org/10.1002/aenm.201300816.
29. Tang, B., Guoxin, H., and Gao, H. (2010). Raman Spectroscopic Characterization of Graphene. Appl. Spectrosc. Rev. *45*, 369–407. https://doi.org/10.1080/05704928.2010.483886.
30. Ferrari, A.C., and Basko, D.M. (2013). Raman spectroscopy as a versatile tool for studying the properties of graphene. Nat. Nanotechnol. *8*, 235–246. https://doi.org/10.1038/nnano.2013.46.
31. Muzyka, K., and Xu, G. (2022). Laser-induced graphene in facts, numbers, and notes in view of electroanalytical applications: A review. Electroanalysis *34*, 574–589. https://doi.org/10.1002/elan.202100425.
32. Pope, C.G. (1997). X-Ray diffraction and the Bragg equation. J. Chem. Educ. *74*, 129–131. https://doi.org/10.1021/ed074p129.
33. Bhattacharjya, D., Kim, C.H., Kim, J.H., You, I.K., In, J.B., and Lee, S.M. (2018). Fast and controllable reduction of graphene oxide by low-cost CO2 laser for supercapacitor application. Appl. Surf. Sci. *462*, 353–361. https://doi.org/10.1016/j.apsusc.2018.08.089.
34. Kim, K.Y., Choi, H., Tran, C.V., and In, J.B. (2019). Simultaneous densification and nitrogen doping of laser-induced graphene by duplicated pyrolysis for supercapacitor applications. J. Power Sources *441*, 227199. https://doi.org/10.1016/j.jpowsour.2019.227199.
35. De La Roche, J., López-Cifuentes, I., and Jaramillo-Botero, A. (2023). Influence of lasing parameters on the morphology and electrical resistance of polyimide-based laser-induced graphene (LIG). Carbon Lett. *33*, 587–595. https://doi.org/10.1007/s42823-022-00447-2.
36. Le, T.-S.D., Phan, H.-P., Kwon, S., Park, S., Jung, Y., Min, J., Chun, B.J., Yoon, H., Ko, S.H., Kim, S.-W., and Kim, Y.-J. (2022). Recent advances in laser-induced graphene: mechanism, fabrication, properties, and applications in flexible electronics. Adv. Funct. Mater. *32*, 2205158. https://doi.org/10.1002/adfm.202205158.
37. Murray, R., Burke, M., Iacopino, D., and Quinn, A.J. (2021). Design of experiments and optimization of laser-induced graphene. ACS Omega *6*, 16736–16743. https://doi.org/10.1021/acsomega.1c00309.
38. Peng, Z., Ye, R., Mann, J.A., Zakhidov, D., Li, Y., Smalley, P.R., Lin, J., and Tour, J.M. (2015). Flexible Boron-Doped Laser-Induced Graphene Microsupercapacitors. ACS Nano *9*, 5868–5875. https://doi.org/10.1021/acsnano.5b00436.
39. Liu, T., Ren, R., Qi, Z., Hu, J., Chen, Y., Huang, Y., Guo, Y., Cao, H., Liang, M., Sun, J., et al. (2024). High-performance micro supercapacitor assembled by laser-induced graphene electrode and hydrogel electrolyte with excellent interfacial wettability for high capacitance. J. Power Sources *602*, 234307. https://doi.org/10.1016/j.jpowsour.2024.234307.
40. Peng, Z., Lin, J., Ye, R., Samuel, E.L.G., and Tour, J.M. (2015). Flexible and Stackable Laser-Induced Graphene Supercapacitors. ACS Appl. Mater. Interfaces *7*, 3414–3419. https://doi.org/10.1021/am509065d.
41. Parmeggiani, M., Zaccagnini, P., Stassi, S., Fontana, M., Bianco, S., Nicosia, C., Pirri, C.F., and Lamberti, A. (2019). PDMS/Polyimide Composite as an Elastomeric Substrate for Multifunctional Laser-Induced Graphene Electrodes. ACS Appl. Mater. Interfaces *11*, 33221–33230. https://doi.org/10.1021/acsami.9b10408.
42. Zhang, Z., He, B., Han, Q., He, R., Ding, Y., Han, B., and Ma, Z.-C. (2023). Femtosecond Laser Direct Writing of Gecko-Inspired Switchable Adhesion Interfaces on a Flexible Substrate. Micromachines *14*, 1742. https://doi.org/10.3390/mi14091742.
43. Grazulis, S., Daskevic, A., Merkys, A., Chateigner, D., Lutterotti, L., Quirós, M., Serebryanaya, N.R., Moeck, P., Downs, R.T., and Le Bail, A. (2012). Crystallography Open Database (COD): an open-access collection of crystal structures and platform for world-wide collaboration. Nucleic. Acids. Res. *40*, D420–D427. https://doi.org/10.1093/nar/gkr900.
44. Schneider, C.A., Rasband, W.S., and Eliceiri, K.W. (2012). NIH Image to ImageJ: 25 years of image analysis. Nat. Methods *9*, 671–675. https://doi.org/10.1038/nmeth.2089.
45. Conway, B.E. (1999). Electrochemical Supercapacitors: Scientific Fundamentals and Technological Applications (Springer). https://doi.org/10.1007/978-1-4757-3058-6.

STAR★METHODS

KEY RESOURCES TABLE

REAGENT or RESOURCE	SOURCE	IDENTIFIER
Chemicals, peptides, and recombinant proteins		
Kapton film. Polyimide with silicone adhesive	Tesa	Tesa® 51408
Kapton film. Polyimide	Dupont	Dupont™ Kapton® 500HN
Poly(vinyl alcohol) (PVA) M_w 85.000-124.000, 87%-89% hydrolyzed	Sigma-Aldrich	363081 CAS: 9002-89-5
Sulfuric acid, H_2SO_4, 95%-97% EMSURE® ISO	Supelco	1007310510 CAS: 7664-93-9
Polydimethylsiloxane (PDMS)	Dow	SYLGARD™ 184 Silicone Elastomer Kit Curing agent CAS: 2554-06-5 Base CAS: 100-41-4
Software and algorithms		
Image J	https://imagej.net/ij/	https://doi.org/10.1038/nmeth.2089
OriginLab	https://www.originlab.com/	OriginPro 8.5.0

METHOD DETAILS

Materials

In this work, laser-induced graphene was produced using an infrared continuous wave CO_2 laser cutter machine with a wavelength of 10.6 μm, a maximum power of 40 W, and a scan speed of up to 600 mm/s (VEVOR® company, Germany). Commercial polyimide in the form of 125 μm thick Kapton film (DuPont™ Kapton® HN, USA) was used as the precursor material to transform it into LIG. Silver paint (RS PRO, UK), copper tape (RS PRO, UK), and 60 μm thick adhesive Kapton film (Tesa®, Norderstedt, Germany) were used to assemble the device. For the fabrication of the gel electrolyte, polyvinyl alcohol (PVA) (Sigma-Aldrich, 87-89% hydrolyzed medium molecular weight, USA) and sulfuric acid (H_2SO_4) (EMSURE®, sulfuric acid 95-97%, Germany) were employed.

LIG electrodes characterization methods

In all the characterization methods, the six types of samples described above, and summarized in Table S1 (supplemental information) were measured: sLIG-2.0, sLIG-2.4, sLIG-2.8, dLIG-2.0, dLIG-2.4, and dLIG-2.8.

An optical microscope (Leica DMRX, Germany) was used to measure the width of the electrode fingers and the gap distance between them. The morphology of the fabricated laser-induced graphene structures was characterized by scanning electron microscopy (FEI inspect F50), with an accelerating voltage of 5 kV. LIG squares with an area of 4 x 5 mm^2 were measured, on which an electrical path was introduced using silver paint and copper tape to mitigate charging effects.

Raman analysis with a LabRam HR Evolution spectrometer (λ = 532 nm, Horiba, Japan) was performed on LIG strips with an area of 5 x 15 mm^2. The spectra were taken with a magnification lens of ×10, an ND filter of 50%, 5 accumulations, and an acquisition time of 20 s.

X-Ray Diffraction (XRD) analysis was carried out by means of a X'Pert PRO (Malvern-Panalytical) diffractometer using Co Kα radiation (λ=1.789 Å). The instrument was configured with Bragg-Brentano geometry, employing operation parameters of 40 kV and 40 mA. The diffractograms were acquired in the 5–90° (2θ) range, with a step size of 0.01° (2θ). Identification of the samples was carried out by using the information available at the Crystallography Open Database (COD)[43] and the International Centre for Diffraction Data (ICDD).

The specific surface area (SSA) of the samples was determined by Brunauer–Emmett–Teller (BET) technique with an ASAP 2020 (Micromeritics, Norcross, GA, USA). In addition, the distribution of pores sizes from the N_2 adsorption-desorption isotherms was evaluated by Barrett-Joyner-Halenda (BJH) method.

For XRD and SSA characterization, 200 mg of each of the LIG samples were obtained by gently peeling off the material from the substrate to collect it as powder.

In order to determine the sheet resistance of the samples, four-point probe measurements were performed with a Karl Suss PSM 6 probe station and an Agilent 4156C analyzer. For each of the six studied conditions, three samples were fabricated and measured to provide a mean value with their corresponding standard deviations.

In the wettability tests, for each of the three used laser powers: 2.0, 2.4, and 2.8 W, two adjacent LIG squares were fabricated, corresponding to single and double passes, respectively. A 1 ml DI water droplet was dispensed onto the surface of each LIG area, and pictures were taken immediately after. Water contact angles were then estimated using ImageJ software.[44]

Supercapacitors electrochemical characterization

To assess the electrochemical performance of the MSCs, cyclic voltammetry (CV) and galvanostatic charge-discharge (GCD) measurements within a voltage range of 0-1 V were executed utilizing a potentiostat/galvanostat system (Autolab PGSTAT204, Metrohm, Switzerland) along with Nova software. For electrochemical impedance spectroscopy (EIS) measurements, a FRA32M frequency response analyzer module of the PGSTAT204 system was employed. During EIS running, a sinusoidal signal with 10 mV of amplitude was applied at an open circuit, covering a frequency range from 100 kHz to 10 mHz. All measurements were carried out under ambient conditions.

From the GCD results, the areal values of capacitance (mF/cm^2), energy density (μWh/cm^2), power density (mW/cm^2), and equivalent series resistance (ohms) were calculated, respectively, as:[45]

$$C_A = \frac{I_{discharge}}{S \times \left(dV/dt\right)} \quad \text{(Equation 1)}$$

where $I_{discharge}$ corresponds to the constant discharge current, S is the total area of both electrodes, and dV/dt represents the slope of the discharge curves.

$$E_A = \frac{1}{2} \times C_A \times \frac{(\Delta V)^2}{3.600} \quad \text{(Equation 2)}$$

where $\Delta V = V_{max} - V_{drop}$ is the discharge voltage, being V_{max} =1 V for the electrolyte used in this work. V_{drop} represents the voltage difference between V_{max} and the next point in the discharge curve.

$$P_A = \frac{E_A}{\Delta t} \times 3.600 \quad \text{(Equation 3)}$$

where Δt corresponds to the discharge time (s).

$$ESR = \frac{V_{drop}}{2I} \quad \text{(Equation 4)}$$

which represents the voltage drop produced after changing the current polarity from positive to negative.

To bend the MSCs under different controlled angles, three aluminum blocks with angles of 30°, 60°, and 90°, were used. The blocks were completely covered with the adhesive Kapton film to insulate them electrically from the MSCs.

Process of LIG transfer to PDMS substrate

A mixture of prepolymer and curing agent (SYLGARD™ 184 silicone elastomer kit, Dow, US) in a 10:1 ratio was stirred for 10 min until a clear and transparent mixture was observed. Then, the mixture was placed under vacuum until the air bubbles trapped inside were removed. Subsequently, the mixture was carefully poured into a home-made aluminum mold containing the LIG samples on the Kapton substrate. Then, the mold and its contents underwent another vacuum treatment to eliminate any remaining air. Finally, during the curing step, the entire assembly was placed in an oven at 55-65°C for 2 hours.

QUANTIFICATION AND STATISTICAL ANALYSIS

In the figures, both in the main text and in the supplemental file, the graphs were generated using OriginPro 8.5.0 from the raw data. In Figure S3, the water contact angles were estimated using ImageJ after the wettability tests. In Figure 4F, regarding the sheet resistance of the LIGs, each point corresponds to an average value of three samples, including their standard deviation represented as the vertical error bars. The average and the standard deviation are performed by the Origin software and represented as a graph.